

## RESEARCH ARTICLE

10.1002/2017JD027086

## Key Points:

- LES simulations are used to study the cloud topped boundary layer responses to sea ice cover variability near the sea ice margin area
- Change of sea ice cover amount modifies the relative strength of turbulent sources and the upward advection of water vapor into the clouds
- Simulations with smaller sea ice cover amounts are associated with more cloud ice but not necessarily more cloud liquid

## Correspondence to:

Z. Li,  
zhujunlizhujun@gmail.com

## Citation:

Li, Z., Xu, K.-M., & Cheng, A. (2017). The response of simulated arctic mixed-phase stratocumulus to sea ice cover variability in the absence of large-scale advection. *Journal of Geophysical Research: Atmospheres*, 122, 12,335–12,352. <https://doi.org/10.1002/2017JD027086>




Received 5 MAY 2017

Accepted 27 OCT 2017

Accepted article online 3 NOV 2017

Published online 22 NOV 2017

## The Response of Simulated Arctic Mixed-Phase Stratocumulus to Sea Ice Cover Variability in the Absence of Large-Scale Advection

Zhujun Li<sup>1</sup> , Kuan-Man Xu<sup>1</sup> , and Anning Cheng<sup>2</sup> 

<sup>1</sup>NASA Langley Research Center, Hampton, VA, USA, <sup>2</sup>EMC/NOAA Center for Weather and Climate Prediction, College Park, MD, USA

**Abstract** This study examines the responses of Arctic mixed-phase stratocumulus boundary layer to sea ice cover variability near the sea ice margins using large eddy simulations. The simulations are conducted for two different atmospheric conditions, based on observations from the Surface Heat Budget of the Arctic Ocean Experiment (SHEBA) (100% sea ice-covered) and the Mixed-Phase Arctic Cloud Experiment (M-PACE) (open ocean). The effect of sea ice cover variability is investigated for both atmospheric conditions by conducting a series of simulations prescribed with varying amounts of sea ice cover and no large-scale advection. As sea ice cover amount decreases, the SHEBA boundary layer deepens and becomes decoupled. The relative strength of turbulence driven by surface heating to that driven by cloud top radiative cooling increases. Cloud ice and snow grow more efficiently than cloud liquid with moisture transported from the lower boundary layer. On the other hand, as sea ice cover amount increases, the M-PACE boundary layer becomes shallower and more coupled with the surface as turbulence mainly driven by cloud top radiative cooling. Moisture supply from the surface is reduced, while cloud droplets are generated from turbulence at cloud top with little ice formation. In both atmospheric conditions, the boundary layer turbulence structure is modified according to change in the relative strength of boundary layer turbulent sources as sea ice amount changes, resulting in the growth/decay of the cloud layer. Simulations with smaller sea ice cover amounts are associated with more cloud ice but not necessarily more cloud liquid.

### 1. Introduction

The Arctic sea ice cover is crucial to regional and global climate variability through the ice-albedo feedback, and the Arctic clouds play an important role in the regional radiation budget. The global temperature trend is amplified in the Arctic region (Holland & Bitz, 2003; Serreze et al., 2009), partially because the sea ice melting exposes larger areas of ocean to solar radiation, causing further temperature increase, ice melting, and surface flux enhancement (e.g., Perovich et al., 2008; Serreze & Francis, 2006). The cloud-related processes, especially those of low-level mixed-phase clouds, are considered crucial to the accelerated ice decline, due to their impact on the Arctic surface energy budget (Bennartz et al., 2013; Francis & Hunter, 2006).

As a substantial contributor to Arctic low cloud fraction, persistent Arctic mixed-phase stratocumulus (AMPS) clouds are observed to occur frequently, especially during the spring and autumn transition seasons (Shupe, 2011). The boundary layer turbulence plays a key role in modulating the AMPS cloud properties and thermodynamic structure (see review by Morrison et al., 2012). In addition, it has been noticed that changes in large-scale advection could cause the transition of an AMPS boundary layer between coupled and decoupled states (Shupe et al., 2013; Sotiropoulou et al., 2014), and the entrainment of moist air at cloud top may prolong the cloud lifetime for some long-lived AMPS clouds (Morrison et al., 2012; Solomon et al., 2011). In the absence of large-scale advection of moisture over the cloud top, the change of sea ice cover amount is one of the most important factors for the evolution of AMPS boundary layer. Over 100% sea ice cover, the turbulence generated by the surface has little impact on AMPS cloud processes, compared to that generated from the cloud top cooling as the cloud topped boundary layer is fully coupled. In contrast, the change of sea ice cover amount may significantly alter the AMPS boundary layer, for example, deepening the boundary layer and decoupling the cloud layer from the surface, due to the increase in surface temperature and turbulent fluxes as sea ice cover amount decreases.

The sensitivity of AMPS clouds to the changing sea ice cover amount is often difficult to diagnose from observations, since different data sets and analysis methods may yield inconsistent results. For example,

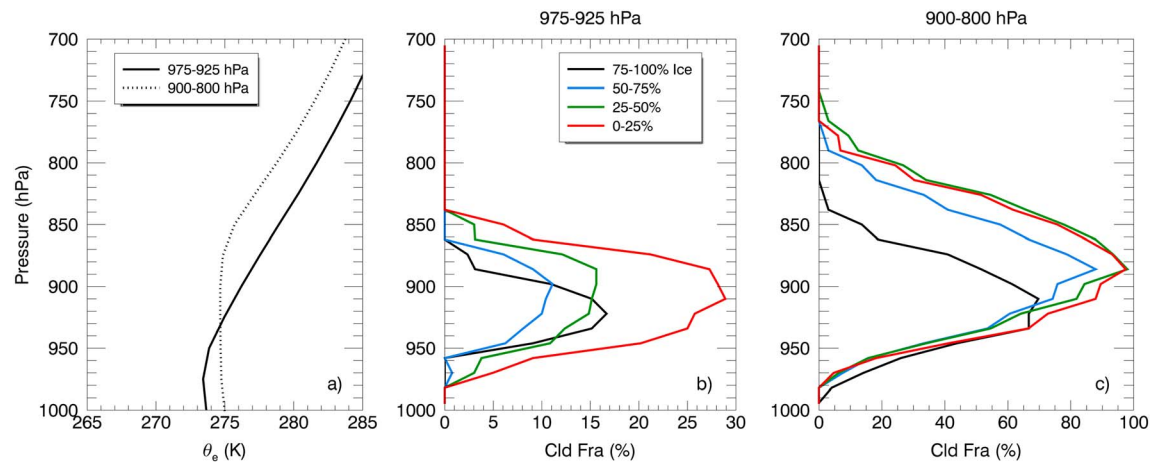


**Figure 1.** Satellite retrievals from July 2006 to June 2010, between 70°N and 81°N; (a) median profiles of equivalent potential temperature ( $\theta_e$ ) from MERRA for the atmosphere containing well-mixed boundary layer with top heights between 975–925 hPa and 900–800 hPa; (b and c) median profiles of cloud fraction from the C3M data set sorted by sea ice cover amount for the shallow and deep well-mixed boundary layer in Figure 1a.

examination of reanalysis data indicates that sea ice retreat is associated with a decrease in low-level cloud amount, since cloud layer rises due to the change of vertical temperature structure (Schweiger et al., 2008). However, active-sensor satellite observations show that cloud amount decreases for clouds below the 500 m level and increases for higher clouds between 800 and 1,800 m during the period of sea ice melting (Palm et al., 2010). Climate model projections show that the sea ice decline in autumn is associated with more low cloud amount, more liquid in cloud, and thus higher cloud emissivity (Vavrus, Holland, & Bailey, 2011). Field campaigns over the sea ice margin areas could identify the decoupling states to the depth of the boundary layer but were unable to attribute the different states to changes in surface fluxes or sea ice cover amounts (Sotiropoulou et al., 2014).

### 1.1. Satellite Data Evidence

We first perform an exploratory analysis, in order to estimate the relationship between sea ice extent, cloud cover, and boundary layer structure, using satellite observations and reanalysis over the region bounded by the 70°N and 81°N latitudinal bands. Collocated satellite properties, for the July 2006 to June 2010 period, are taken from the Cloud-Aerosol Lidar and Infrared Pathfinder Satellite Observation (CALIPSO), CloudSat, Clouds and the Earth's Radiant Energy System (CERES), Moderate Resolution Imaging Spectroradiometer (MODIS), denoted as C3M, merged data set (Kato et al., 2010), with a horizontal resolution of approximately 20 km (CERES instrument footprint) and a vertical resolution of 120 m. The C3M data set has been previously used in Taylor et al. (2015) to examine the relationship between Arctic cloud properties and sea ice cover amount according to the seasonality and lower tropospheric stability. In addition, we utilize equivalent potential temperature ( $\theta_e$ ) profiles from the Modern Era Retrospective Analysis for Research and Applications (MERRA) (Rienecker et al., 2011) to explore changes in the boundary layer. This analysis is limited to well-mixed boundary layer profiles only, defined as those with  $\theta_e$  vertical changes of less than 1 K within the boundary layer. The profiles are further classified into “shallow” and “deep” boundary layers according to their inversion heights, with heights between 975–925 hPa and 900–800 hPa, respectively (Figure 1a). For each boundary layer type, the median cloud fraction is computed from satellite data for varying values of sea ice cover, which is in turn derived from the Special Sensor Microwave Imager (Cavalieri, Gloersen, & Zwally, 1990).

The median cloud fraction profile for the shallow boundary layer (Figure 1b) depicts modest but noticeable changes with sea ice cover amounts. Namely, both the median cloud fraction at levels above 900 hPa and cloud top height generally increase as sea ice cover amount decreases. This increase becomes more evident for the deep boundary layer case (Figure 1c) except for minimal differences between the two lowest sea ice cover bins. Overall, this preliminary analysis shows significant differences in cloud structure and height that are associated with changes in sea ice cover amount for both shallow and deep boundary layers.

## 1.2. Objective of This Study

This study is motivated by the results from Figure 1, Sotiropoulou et al. (2014), and Taylor et al. (2015) but does not intend to replicate the observed atmospheric conditions in these studies. The main goal of this study is to understand the changes in the dynamical and thermodynamic structure of the AMPS boundary layer and the changes of cloud properties such as cloud amount, height, and thickness in response to the variability in sea ice cover amount. This study addresses the following questions. How is the decoupling of the boundary layer related to changes in surface temperature and sea ice cover amount? How does the relative strength of turbulent sources on the surface and cloud top impact the boundary layer response to sea ice cover change? What roles do cloud microphysical processes play in this response?

In this study, a modeling approach is selected in order to avoid the limitations of scarce observational data. We will use the large eddy simulation (LES) approach, which has the advantage of resolving boundary layer turbulence while isolating the sea ice cover variability from other factors by controlling the initial conditions and the large-scale advection. A series of simulations are performed, based upon two distinct atmospheric conditions. They are constructed from observations from field experiments. We perform 4-day long LES integrations to obtain the equilibrium response to sea ice variations. The turbulent kinetic energy (TKE) budget and cloud microphysical budget will be analyzed to help addressing the proposed questions and achieve the goal of this study.

## 2. Model Description and Simulation Setup

### 2.1. Model Description

The System for Atmospheric Modeling (SAM) model (Khairoutdinov & Randall, 2003) version 6.10.6 is used for the simulations performed in this study. SAM is a nonhydrostatic anelastic model that has been previously used to study boundary layer clouds (e.g., Fan et al., 2009; Stevens et al., 2005), with a monotonic advection algorithm (Smolarkiewicz & Grabowski, 1990), and a Smagorinsky-type subgrid-scale parameterization. Radiation is calculated using the Rapid Radiation Transfer Model package exported from the National Center for Atmospheric Research Community Earth System Model (Collins et al., 2004). The model has periodic lateral boundaries and a rigid lid for the domain top, with damping applied in the upper third of the domain to reduce spurious gravity wave reflection.

This study uses the double-moment Morrison microphysical scheme (Morrison, Curry, & Khvorostyanov, 2005), which predicts cloud droplet, ice, rain, graupel, and snow mass mixing ratios and number concentrations. The aerosol size follows the bimodal distribution (Morrison et al., 2008),

$$\frac{dN}{d \ln r} = \frac{N_t}{\sqrt{2\pi} \ln \sigma} \exp \left[ -\frac{\ln^2(r/r_m)}{2 \ln^2 \sigma} \right]$$

where  $\sigma$  is the geometric standard deviation,  $r_m$  is the mean aerosol radius, and  $N_t$  is the total number concentration of each mode of the distribution. These parameters are prescribed for the smaller mode as 2.04, 0.052  $\mu\text{m}$ , and 350  $\text{cm}^{-3}$  (adjusted to 72.2  $\text{cm}^{-3}$  for the Mixed-Phase Arctic Cloud Experiment case described later to better match with the observations), and for the larger mode as 2.5, 1.3  $\mu\text{m}$  and 1.8  $\text{cm}^{-3}$ , respectively.

The surface sensible heat flux (SHF) and latent heat flux (LHF) are calculated locally based on the surface winds, temperature, and humidity. The heat and moisture transfer coefficients in the bulk formula for both ocean and sea ice grid points are adapted from Large and Pond (1982), while the surface stress coefficient follows Geleyn (1988). In addition, the ocean surface albedo is calculated as a function of solar zenith angle, but it is prescribed over sea ice as 0.45 and 0.75 for wavelengths between 0.7 and 5  $\mu\text{m}$  and between 0.2 and 0.7  $\mu\text{m}$ , respectively.

### 2.2. Case Overview

Two cases are selected for this study, representing two very different synoptic underlying surface conditions in the Arctic region during the transitions in spring and autumn, respectively. One is based on the observations on 7 May 1998 from the Surface Heat Budget of Arctic Ocean (SHEBA) and First International Satellite

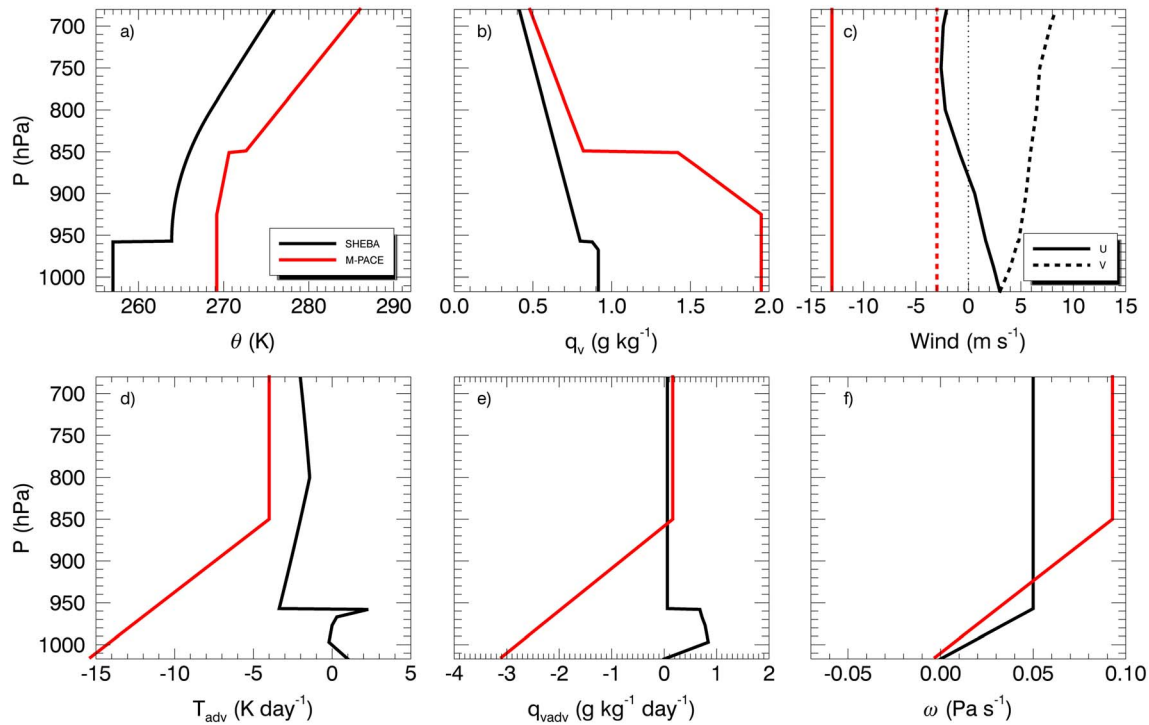


**Figure 2.** Initial profiles of (a) potential temperature ( $\theta$ ), (b) water vapor mixing ratio ( $q_v$ ), (c) zonal (solid) and meridional (dashed) winds, large-scale horizontal advection of (d) temperature and (e) water vapor mixing ratio, and (f) large-scale pressure velocity ( $\omega$ ), for the SHEBA (black) and the M-PACE (red) reference simulations.

Cloud Climatology Project Regional Experiment-Arctic Cloud Experiment (Uttal et al., 2002). The observations of this case have been presented and discussed in Zuidema et al. (2005), Morrison, Zuidema, Ackerman, et al. (2011), Morrison, Zuidema, Mcfarquhar, et al. (2011) (hereafter referred to as *MO11*), and Fridlind et al. (2012). These observations were collected on an icebreaker ship frozen into the Beaufort Sea ice at 76°N, 165°W, when a broad low-level high-pressure system dominated the region. A boundary layer cloud deck was persistent with a strong temperature inversion of 5–6 K over a depth of ~70 m and a relatively well-mixed boundary layer below. The other case is based on the observations on 9 and 10 October 2004, during the Mixed-Phase Arctic Cloud Experiment (M-PACE) (Verlinde et al., 2007). As described in Verlinde et al. (2007) and Klein et al. (2009) (hereafter referred to as *KL09*), the M-PACE case was constructed based on the observations around the DOE Atmospheric Radiation Measurement Program’s Barrow (71°19’N, 156°36’W) and Oliktok Point site during a cold-air outbreak period. The northeasterly flow around a low level anticyclone located in the north of Alaska transported cold air over the sea ice in the north to the open ocean of Beaufort Sea. Significant surface heat and moisture fluxes due to the cold air above the ocean induced the formation of boundary layer clouds in the form of rolls or cloud streets.

As shown in Figure 2, the M-PACE boundary layer over the open ocean is deeper, warmer, and moister, with strong northeasterly winds and advection of colder and drier air from the north. On the other hand, the SHEBA boundary layer over 100% sea ice cover is significantly colder, drier, and shallower, with weaker southwesterly to southeasterly winds. The magnitudes of horizontal advective warming and moistening within the boundary layer for SHEBA are much smaller than those of horizontal advective cooling and drying for M-PACE (Figures 2d and 2e).

In this study, one reference simulation and five sea ice sensitivity (SIS) simulations prescribed with varying amounts of sea ice cover that range from 0% to 100% at a 25% interval are conducted for SHEBA and M-PACE cases separately. Their setup will be provided in sections 2.3 and 2.4. Hereafter, a simulation with  $x\%$  sea ice cover over the domain is referred to as the  $x\%$  SHEBA/M-PACE simulation. For all simulations, the model horizontal domain size is 3.2 km by 3.2 km, with 25 m by 25 m horizontal grid spacing. The vertical grid spacing is 10 m from surface to 3 km and is stretched to about 80 m from 3 km to the domain top at 6 km. The integration time step is 2 s for all simulations.

**Table 1**

The Surface Temperature, Sensible and Latent Heat Flux, Liquid Water Path (LWP) Including Cloud Liquid and Rain (Cloud Liquid Water Path, CWP), Ice Water Path (IWP) Including Cloud Ice, Snow and Negligible Graupel (Cloud Ice Water Path, CIWP), Surface Precipitation Rate, Cloud Top Entrainment Rate, Longwave Cloud Radiative Effect at the Surface, and Mean Cloud Ice Number Concentration Within AMPS Cloud Layer

		ST (K)	SHF (W m <sup>-2</sup> )	LHF (W m <sup>-2</sup> )	LWP (CWP) (g m <sup>-2</sup> )	IWP (CIWP) (g m <sup>-2</sup> )	PRECIP (mm d <sup>-1</sup> )	We (cm s <sup>-1</sup> )	CRE (W m <sup>-2</sup> )	Ni (L <sup>-1</sup> )
SHEBA	MO11	257.40	7.98	2.86	19.00	4.10	0.37	Na	Na	Na
	Reference	257.40	3.82	0.25	15.03 (15.03)	2.49 (0.70)	0.38	0.27	63.5	2.6
	0%	274.01	20.17	34.98	19.65 (19.65)	36.92 (6.05)	0.40	0.72	38.2	2.2
	25%	271.35	16.54	27.30	16.71 (16.70)	28.78 (5.47)	0.35	0.37	44.0	2.8
	50%	268.74	18.18	23.68	18.80 (18.80)	16.26 (2.90)	0.23	0.47	58.8	2.3
	75%	264.17	16.04	16.61	21.17 (21.16)	11.48 (1.99)	0.28	0.37	64.3	3.0
	100%	257.40	-0.79	0.04	0.00 (0.00)	0.03(0.02)	0.00	Na	0.05	0.2
M-PACE	KL09	274.01	136.50	107.7	57.30	17.10	0.41	Na	Na	Na
	Reference	274.01	102.89	105.97	111.22 (109.94)	28.75 (1.60)	0.89	0.90	68.2	1.2
	0%	274.01	1.24	38.66	84.34(83.48)	2.02(0.09)	0.03	0.93	66.7	0.1
	25%	271.35	4.33	40.20	133.60 (131.91)	2.76 (0.06)	0.09	0.52	72.7	0.1
	50%	268.74	9.86	22.63	98.92 (98.17)	1.22 (0.05)	0.07	0.35	76.1	0.1
	75%	264.17	16.00	10.73	60.30 (60.04)	0.72 (0.08)	0.08	0.28	74.9	0.1
	100%	257.40	-0.44	0.18	0.00 (0.00)	0.01 (0.00)	0.00	0.02	0.0	0.0

Note. All values are the averages over the last hour of model output for the reference simulations and the averages of the last 5 h of model output for the SIS simulations. The averages over hour 11.5–12 of the DHARMA simulation in MO11 and the average over hour 4–12 of the median CRMs in KL09 are also shown.

### 2.3. Reference Simulation Setup

The reference SHEBA and M-PACE simulations are intended to replicate the simulations in *MO11* and *KL09*. The simulation setup is identical to *MO11* and *KL09* except that surface fluxes are computed but they are prescribed in *MO11* and *KL09*. Thus, surface fluxes are allowed to change with the underlying surface types and the evolution of the boundary layer. The same initial thermodynamic and dynamical conditions, large-scale advection of heat and moisture, and large-scale subsidence that are derived from the reanalysis data and observations (Figure 2) used in *MO11* and *KL09* are used in these reference simulations. The same surface temperatures, 257.4 K in *MO11* and 274.01 K in *KL09*, are used for the entire domain. The model integration for the reference simulations starts at 1200 UTC, 7 May for SHEBA, and 1700 UTC, 9 October for M-PACE, with the large-scale forcing kept constant and wind nudged toward the prescribed wind profiles at a time scale of 1 h. The integration time is 15 h, instead of 12 h in *MO11* and *KL09*. This integration time is long enough for the surface fluxes to reach magnitudes comparable to the prescribed values in *MO11* and *KL09* (Table 1), but not so long that the thermodynamic profiles drift away from initial values as the large-scale advection persists.

### 2.4. Sea Ice Sensitivity (SIS) Simulation Setup

A series of the SIS simulations are carried out for SHEBA and M-PACE cases separately, beginning with the reference simulation of each case. Four of the five SIS simulations are initiated with the final atmosphere state produced by the simulation with 25% greater (SHEBA) or smaller (M-PACE) sea ice cover amount and integrated for 48 h. The long integration time allows the model to produce nearly equilibrium responses to sea ice and surface temperature variations at the end of each SIS simulation. Specifically, the reference SHEBA and M-PACE simulations are first conducted, then the 75% SHEBA simulation and the 25% M-PACE simulation are initiated with the final state of their reference simulations respectively, and the 50% SHEBA and the 50% M-PACE simulations are initiated with the final state of the 75% SHEBA and the 25% M-PACE simulations, and so on. Such a procedure saves spin-up time for the SIS simulations. The remaining SIS simulations (100% SHEBA and 0% M-PACE), which are different from the respective reference simulations, will be described later.

In the SIS simulations, different sea surface temperatures are prescribed to the designated grid points of “sea ice” and “ocean.” For the 25%, 50%, and 75% simulations, the sea ice surface temperature is prescribed within a square that covers the corresponding percentage of area centered in the domain (e.g., Figure 3a). The decrease/increase of sea ice cover amount is often associated with the increase/decrease of sea ice surface

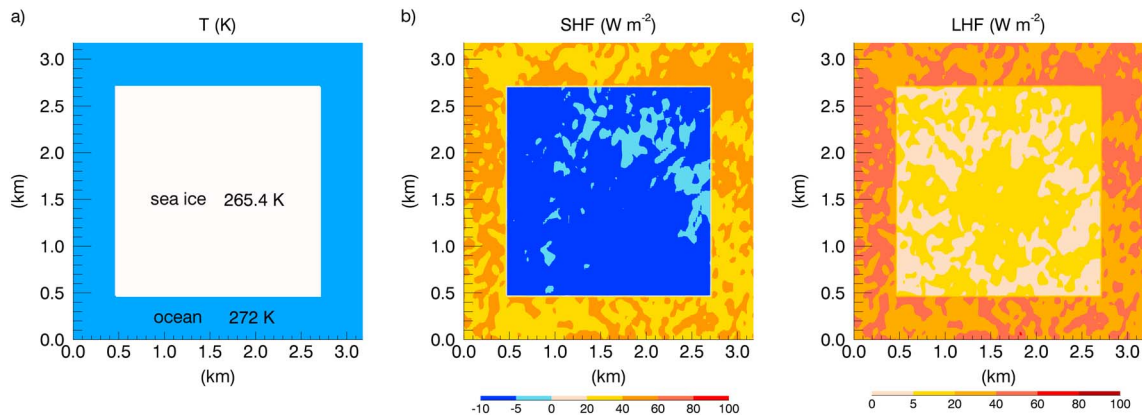


**Figure 3.** For the 50% SHEBA simulation, (a) the prescribed surface temperature, and (b) sensible and (c) latent heat flux at hour 48 of the model output.

temperature, so the prescribed sea ice surface temperature is higher in simulations with smaller sea ice cover amounts. The ice surface temperature is observed at 257.4 K for full ice coverage in May during the SHEBA field experiment (*MO11*) and gradually increases to  $\sim 271$  K as the ice sheets melt during the summer (Uttal et al., 2002). Inferred from observations, the surface temperature of sea ice grid points in the simulations is prescribed at 261.4 K for 75% sea ice cover, 265.4 K for 50%, and 269.4 K for 25%, in both SHEBA and M-PACE cases. The ocean surface temperature is prescribed at 272 K (just above the typical freezing point of seawater) for simulations with sea ice cover of 25%, 50%, and 75%. The surface temperatures of the 0% SHEBA and the 100% M-PACE simulations are specified at 274.01 K and 257.4 K for the entire domain, resembling the reference M-PACE and the reference SHEBA simulations, respectively.

The prescribed surface temperature is expected to impact the SHF and LHF. As an example, Figures 3b and 3c show snapshots of the horizontal distributions of SHF and LHF for the 50% SHEBA simulation. Both SHF and LHF are clearly discrete between ocean and sea ice areas of the model domain: strongly positive over the ocean grid points but weakly positive or negative over the sea ice grid points. The variations in local SHF and LHF for the same type of surface grid points are much smaller than those between the ocean and sea ice surface types. The differences in domain-averaged SHF and LHF among the SIS simulations are mostly due to the different amounts of sea ice cover, especially those of LHF (Table 1).

Another important consideration is how the large-scale horizontal advection profiles should be prescribed in the SIS simulations. For this, we analyzed the large-scale horizontal advection from the MERRA reanalysis data product that are matched to the data set for producing the results shown in Figures 1b and 1c, and little correlation was found between the large-scale horizontal advection and the sea ice cover amount (not shown). Thus, we are left with two choices. We can use the same forcing profiles used in the reference simulations (Figures 2d–2f), which are designed for the 100% sea ice cover (*MO11*) and open ocean (*KL09*) surface conditions. However, as the sea ice cover changes, the surface fluxes change and they can cause significant rise or fall of the boundary layer height, which can result in a significant mismatch with the forcing profiles. It is likely that such a mismatch may not yield consistent responses of the boundary layer to sea ice cover variation. Since the main objective of this study is to investigate the response of cloud topped boundary layer and cloud properties to sea ice cover variability, it is justifiable, for simplicity, to set the large-scale horizontal heat and moisture advection to zero. This simplification means that the LES is put in a quasi-Lagrangian framework (e.g., Krueger, McLean, & Fu, 1995), with large-scale subsidence, sea ice, surface temperature being kept constant for 48 h. After 48 h, the model run continues with a new set of large-scale subsidence, sea ice, and surface temperature in a manner described at the beginning of this section. The remote influence on the responses of the boundary layer to sea ice cover variation is thus excluded in all SIS simulations, but the effect of large-scale horizontal advection will be briefly discussed in section 3.2. For M-PACE, the large-scale pressure velocity ( $\omega$ ) profile is kept the same as the reference simulation for all SIS simulations. The  $\omega$  profile for each SHEBA SIS simulation is adjusted by raising the pressure level at which the large-scale subsidence reaches the maximum by approximately 60 hPa for every 25% increase in sea ice cover amount. This adjustment is intended to maintain the relatively weak large-scale subsidence within the boundary layer compared to that of the free troposphere (Figure 2f).

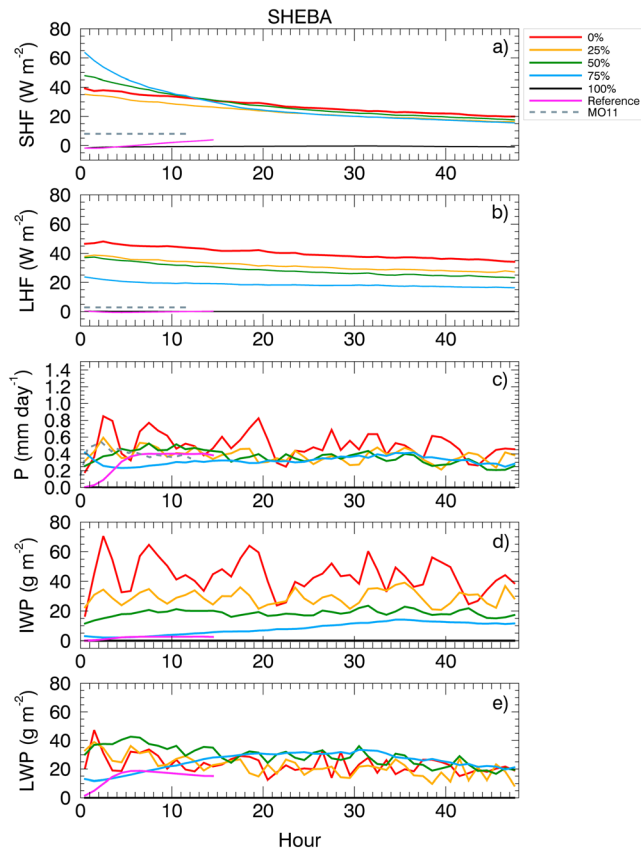


**Figure 4.** Hourly averaged time series for the SHEBA simulations, (a) sensible heat flux, (b) latent heat flux, (c) surface precipitation rate, (d) ice water path, and (e) liquid water path. The colors indicate different simulations. The gray dashed line in Figures 4a and 4b indicates the prescribed surface fluxes in MO11, and the gray dashed line in Figure 4c represents the surface precipitation rate from DHARMA in MO11.

is about 1 K cooler than the DHARMA model output averaged over 11.5 to 12 h, while the boundary layer top height as well as total water mixing ratio ( $q_t$ ) are identical (Figures 5a and 5b). The amounts of cloud liquid and ice are slightly smaller than DHARMA, as reflected in the average cloud liquid water ( $q_c$ ), cloud ice and snow mixing ratio ( $q_i + q_s$ ) profiles (solid profiles in Figures 6a and 6b), and the average LWP and IWP (Table 1 and Figure 6d). The average LWP ( $15.0 \text{ g m}^{-2}$ ) is within the ground-based retrieval values in MO11 that range from 10 to  $40 \text{ g m}^{-2}$ , and the average IWP ( $2.5 \text{ g m}^{-2}$ ) lies between DHARMA and the ground-based range from 0.5 to  $2 \text{ g m}^{-2}$  (Figure 6d). The surface precipitation rate of  $0.38 \text{ mm d}^{-1}$  (Table 1 and Figure 4c) is similar to the DHARMA result ( $0.37 \text{ mm d}^{-1}$ ).

For the reference M-PACE simulation, the average SHF and LHF are  $102.9 \text{ W m}^{-2}$  and  $106.0 \text{ W m}^{-2}$  fluxes, respectively, compared to the European Centre for Medium-Range Weather Forecasts (ECMWF) reanalysis data of  $136.5 \text{ W m}^{-2}$  and  $107.7 \text{ W m}^{-2}$  imposed to simulations in KL09 (Figures 7a and 7b). Although the simulated LHF closely agrees with ECMWF, the simulated SHF is  $33.6 \text{ W m}^{-2}$  lower than ECMWF despite the fact that the simulated boundary layer is  $\sim 1 \text{ K}$  cooler than the initial condition. It is interesting to note that the SHF from ECMWF is much larger than the extreme values from observations conducted over the Arctic open ocean near sea ice margins (e.g., Sotiropoulou et al., 2016).

The average boundary layer characteristics also show substantial differences from those of cloud-resolving model (CRM) ensemble-mean results documented in KL09, but still within the range of all CRMs. Specifically, the average cloud liquid, cloud ice, and snow mixing ratios are greater than the median values of all CRMs in KL09 (Figures 6e and 6f). The average surface precipitation (snow) rate ( $0.89 \text{ mm d}^{-1}$ ) is more than twice of the median snow rate of all CRMs ( $0.41 \text{ mm d}^{-1}$ ) (Figure 7c). The average LWP ( $111.2 \text{ g m}^{-2}$ ) is

The impact of removing the large-scale heat and moisture advection from the SIS simulations is assessed with two additional simulations (100% SHEBA and 0% M-PACE). They use the same setup as the reference simulations, but without large-scale horizontal heat and moisture advection. They are initiated from the same initial states of their respective reference simulations and then integrated for 48 h. Results from comparing these two SIS with reference simulations will be presented in section 3.2. Note that these two simulations were not a part of the quasi-Lagrangian integrations.

### 3. Results

#### 3.1. Reference Simulations

Results from the reference simulations are in reasonable agreement with the simulations analyzed in MO11 and KL09 and the observations reported therein. A detailed comparison of these simulations with MO11 and KL09 is shown below, utilizing the averages over the last hour of the model output.

For the reference SHEBA simulation, the temporal evolution of SHF and LHF is weak due to their small magnitudes (Figures 4a and 4b). The average model-calculated SHF and LHF are  $3.82 \text{ W m}^{-2}$  and  $0.25 \text{ W m}^{-2}$ , compared to the averaged flux tower data of  $7.98 \text{ W m}^{-2}$  and  $2.86 \text{ W m}^{-2}$  reported in MO11. Liquid water path (LWP; including both cloud liquid water and rainwater), ice water path (IWP; including cloud ice, snow, and negligible graupel), and surface precipitation rate reach a quasi-steady state after 5 h (Figures 4c–4e).

The boundary layer characteristics from the reference SHEBA simulation resemble those from the Distributed Hydrodynamic Aerosol and Radiative Modeling Application (DHARMA) (Fridlind et al., 2012) 3-D LES documented in MO11, which uses 50 m horizontal grid spacing, a 3.2 km by 3.2 km domain size, and detailed bin microphysics (Ackerman, Hobbs, & Toon, 1995). The boundary layer liquid water potential temperature ( $\theta_l$ )

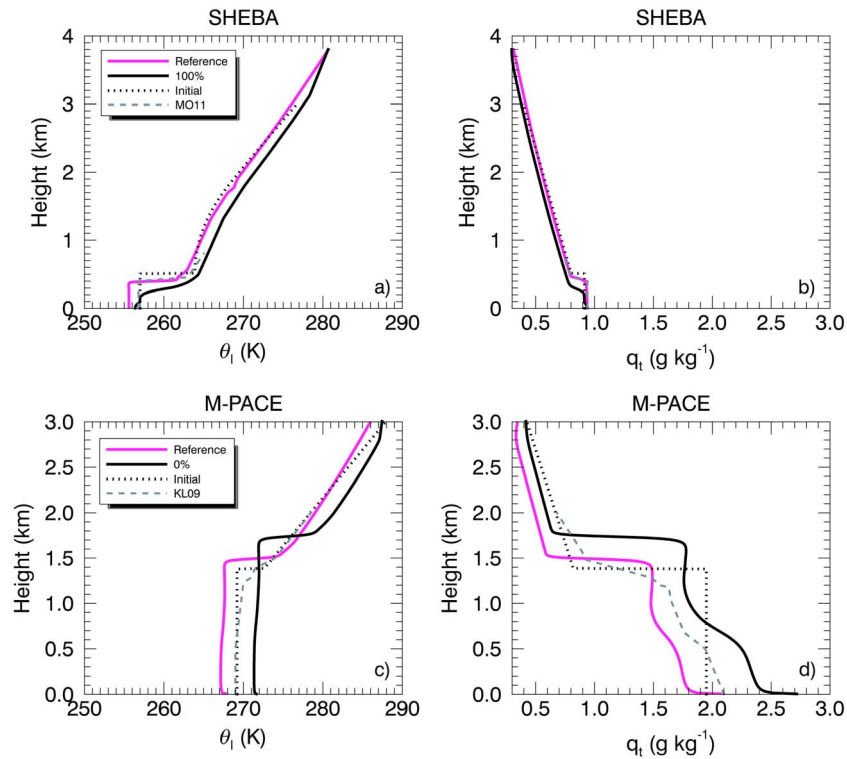


**Figure 5.** Liquid water potential temperature ( $\theta_l$ ) and total water ( $q_t$ ) profiles for the (upper row) SHEBA and (bottom row) M-PACE reference simulations (solid magenta), 100% SHEBA and 0% M-PACE simulations (solid black), averaged over 15 h of model output. The dotted black lines are the initial profiles of the reference SHEBA and M-PACE simulations, and the gray dashed lines are the average of 11.5–12 h from DHARMA in MO11 and the average of 4–12 h from median CRMs in KL09.

only about 10% greater than the median value of the average from 4 to 12 h of the CRM simulations with double-moment microphysics in *KL09* ( $100.0 \text{ g m}^{-2}$ ) but is more than twice of the median value of all CRMs in *KL09* ( $57.3 \text{ g m}^{-2}$ ) and about half of the retrieved values ( $224.2 \text{ g m}^{-2}$  and  $195.6 \text{ g m}^{-2}$ ) (Figure 6h). The average IWP ( $28.8 \text{ g m}^{-2}$ ) is significantly greater than the median value of the CRMs with double-moment cloud microphysics parameterizations ( $19.9 \text{ g m}^{-2}$ ) and all CRMs ( $17.1 \text{ g m}^{-2}$ ) but within the range of retrieved IWPs ( $28.1 \text{ g m}^{-2}$  to  $30.1 \text{ g m}^{-2}$ ; Figure 6h).

The vertical-velocity skewness shows very different characteristics of the turbulent boundary layers between the two reference simulations. In SHEBA, the skewness is positive just below the cloud top but negative in the rest of the boundary layer (Figure 8a). This is typical of the cloud top cooling-driven turbulence and represents a coupled boundary layer (Moeng & Rotunno, 1990). The thin layer near the cloud top with positive skewness has been a mainstay of LES simulations of cloudy boundary layer under a strong inversion. Moeng and Rotunno (1990) explained this by positively buoyant updrafts impinging on the inversion and weak widespread downdrafts just below the inversion. In M-PACE, updrafts generated by surface heating cannot reach all the way to the cloud top and downdrafts generated by radiative cooling cannot reach all the way to the surface. This results in a decoupled boundary layer with a cloud layer of 0.7–0.8 km in thickness (Figure 8b), accompanied by a minimum turbulent kinetic energy (TKE) near the cloud base (Figures 6e and 6g).

### 3.2. Impact of Large-Scale Horizontal Advection

The SHEBA (*MO11*) and M-PACE (*KL09*) intercomparison cases were designed to produce quasi-steady thermodynamic profiles above the boundary layer that resemble the initial conditions. This is evidenced from a comparison between the initial conditions and the profiles at 15 h of the reference simulations (Figure 5), especially for SHEBA. For the free atmosphere, the horizontal advection is balanced by the vertical advection of the moisture and heat (plus radiative cooling) in the budget equations. Note that the large-scale vertical



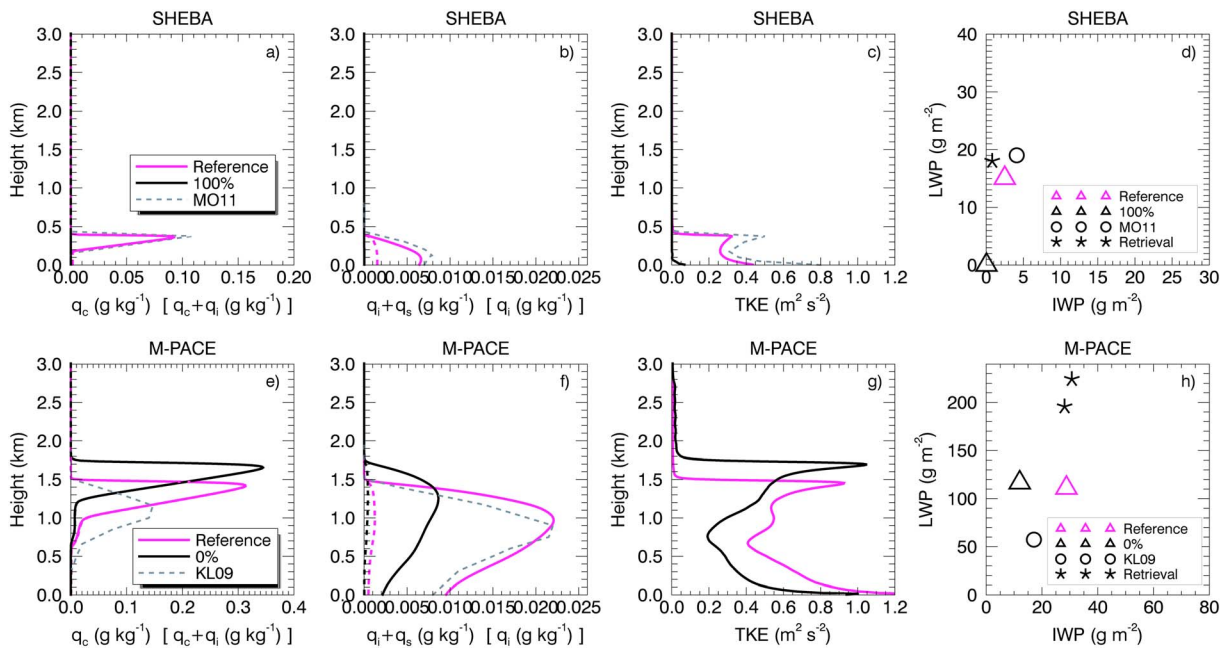


**Figure 6.** For the (upper row) SHEBA and (bottom row) M-PACE simulations, (a and e) the cloud liquid water mixing ratio ( $q_c$ ) (solid), cloud liquid and ice mixing ratio ( $q_c + q_i$ ) (dashed); (b and f) cloud ice and snow mixing ratio ( $q_i + q_s$ ) (solid), cloud ice water mixing ratio ( $q_i$ ) (dashed); (c and g) the resolved turbulent kinetic energy; (d and h) the domain-mean liquid water path as a function of domain-mean ice water path. The reference simulations for SHEBA and M-PACE (solid magenta), 100% SHEBA and 0% M-PACE simulations (solid black) are averaged over the hour 15 of model output. The gray dashed profiles in Figures 6a to 6c and the black circles in Figure 6d indicate the average of 11.5–12 h from DCHARMA in MO11. The gray dashed profiles in Figures 6e and 6f and the black circle in Figure 6h indicate 4–12 h from median CRMs in KL09. In Figures 6d and 6h, the triangles are results from our simulations, the stars indicate the ground-based retrieval values reported in MO11, and the retrievals at Barrow reported in KL09.

velocity is prescribed but the model can adjust the vertical gradients of potential temperature and water vapor mixing ratio to achieve a new balance once the horizontal advection is removed. This can directly impact the boundary layer. Thus, the equilibrium profiles can be drastically different from the initial conditions.

Due to their large magnitudes in the boundary layer of M-PACE (Figures 2d and 2e), the removal of horizontal advective cooling and drying tendencies results in much warmer (4 K) and moister ( $0.3\text{--}0.6\ g\ kg^{-1}$ ) boundary layer. The free atmosphere also undergoes similar changes except with smaller magnitudes. Thus, the inversion strength is slightly stronger than in the reference simulation. The warmer and moister boundary layer results in much smaller SHF and LHF; that is, SHF is reduced from  $103\ W\ m^{-2}$  to  $1.2\ W\ m^{-2}$ , while LHF is reduced from  $106\ W\ m^{-2}$  to  $39\ W\ m^{-2}$  (Table 1). The reduction in SHF and LHF occurs mostly in the first 24 h of the integration as the boundary layer responds to the removal of horizontal advection. The boundary layer top, cloud top, and base are higher by  $\sim 200\ m$  at 15 h (Figures 5c, 5d, and 5e). Due to the reduction of LHF, LWP is reduced by 24% but IWP is reduced from  $29\ g\ m^{-2}$  to  $2\ g\ m^{-2}$ . This result may be related to the increases of ice sublimation (Savre et al., 2015) and stronger decoupling. The latter is seen from the vertical profiles of TKE with minima at  $\sim 0.7\ km$  (Figure 6g). In addition, the stronger inversion also increases the strength of TKE source at the cloud top relative to that of the surface. This point will be further discussed when the SIS simulations are compared in section 3.3.

Because of the much smaller magnitudes in SHEBA, the removal of horizontal advective cooling (above the boundary layer top) and moistening tendencies (within the boundary layer; Figures 2d and 2e) has relatively small impact to potential temperature ( $\sim 1.5\ K$ ) and total water mixing ratio ( $< 0.1\ g\ kg^{-1}$ ) at 15 h. However, the lack of moistening sources from horizontal advection and surface LHF results in the dissipation of the cloud layer and a very thin boundary layer (Figures 6a–6c). The collapsing of the cloud layer eliminates the TKE source at the boundary layer top. A thin layer of mechanical-driven turbulence remains (Figure 6c). As sea ice cover amount increases, surface LHF increases, which provides a moisture source for cloud formation in the SIS simulations. Thus, moistening due to horizontal advection is an important source for the maintenance of Arctic clouds over ice-covered surface.

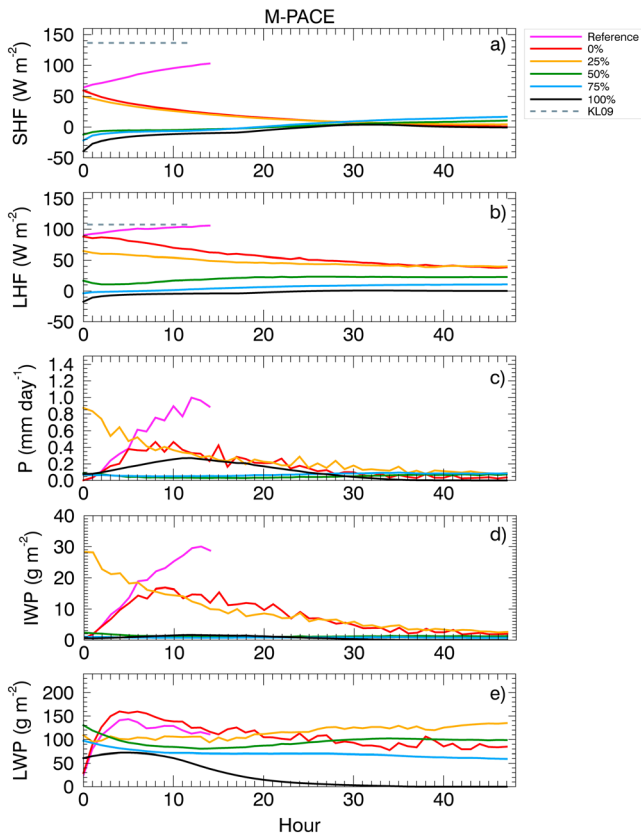


**Figure 7.** Same as Figure 4, but for the M-PACE simulations. (a and b) The gray dashed line indicates the prescribed surface fluxes in KL09.

**3.3. Sea Ice Sensitivity Simulations**

The responses of cloud topped boundary layer and cloud properties to the change of sea ice cover amount are analyzed in this section. Although the SIS simulations do not reach equilibrium, the temporal evolutions of surface fluxes, precipitation, IWP, and LWP become much steadier toward the end of integration compared to the first 10 h (Figures 4 and 7). Therefore, averages from the 44 to 48 h of the model output are obtained for this discussion.

**3.3.1. Boundary Layer Response to the Change of Sea Ice Cover Amount**

As the amount of sea ice cover changes for both sets of quasi-Lagrangian simulations, the boundary layer of a new SIS simulation adjusts to the sea ice surface temperature and surface SH and LH fluxes evolve with the changes in the boundary layer (Figures 4a and 4b and 7a and 7b). At the nearly equilibrium states (the averaging period of 44 to 48 h), one can see that in both the SHEBA and M-PACE experiments, smaller sea ice cover amount always corresponds to greater boundary layer temperature and moisture content, higher boundary layer height, smaller potential temperature jump at the inversion (Figure 9), and greater cloud top entrainment rate (Table 1; except for 25% SHEBA simulation). Both the 100% SHEBA and M-PACE simulations produce very shallow boundary layers, related to the collapse of cloud layer resulting from the lack of moisture source, as discussed in section 3.2. For the same sea ice cover amount, the higher boundary layer heights in the SHEBA simulations reflect the weaker large-scale subsidence (Figure 2f) and the more strongly decoupled states of the boundary layers, compared to the M-PACE simulations. Observations showed that clouds with tops below 700 m tend to get coupled to the surface, whereas those whose tops are above 900 m remain decoupled from it (Sotiropoulou et al., 2014). Although the potential temperature is well mixed in the boundary layer, there are large gradients in the moisture profiles, especially in the subcloud layers of all SHEBA simulations and the 0% M-PACE simulation. This feature was observed in the decoupled boundary layers (Sotiropoulou et al., 2014).

In the following, the results of the SHEBA SIS simulations will be discussed first then compared to the M-PACE counterpart. For the SHEBA simulations, the inversion and cloud top height deepen from 1.2 km (75% sea ice), 1.6 km (50% sea ice), and 2.0 km (25% sea ice) to 2.4 km (sea ice free) as the sea ice cover amount

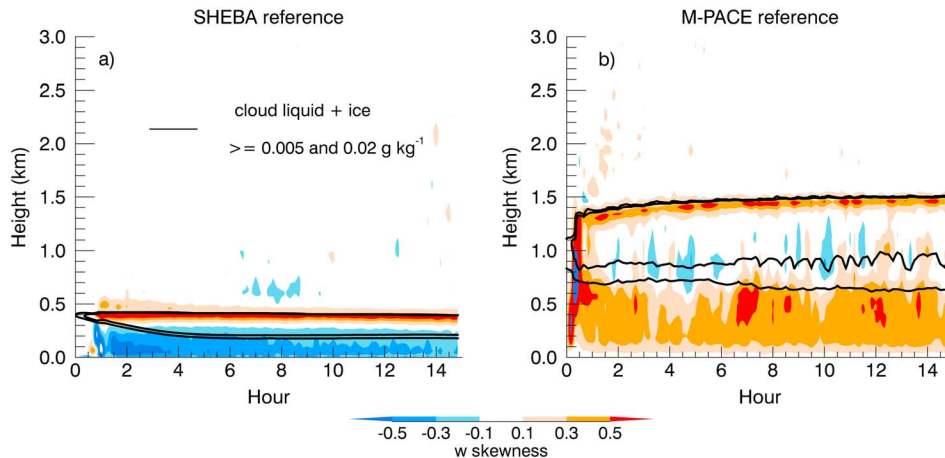


**Figure 8.** For the (a) SHEBA and (b) M-PACE reference simulations, the temporal evolution of domain-mean cloud liquid and ice water mixing ratio profile (outer black contour indicates  $0.005 \text{ g kg}^{-1}$ ; inner black contour indicates  $0.02 \text{ g kg}^{-1}$ ), as well as the vertical velocity skewness (color shaded).

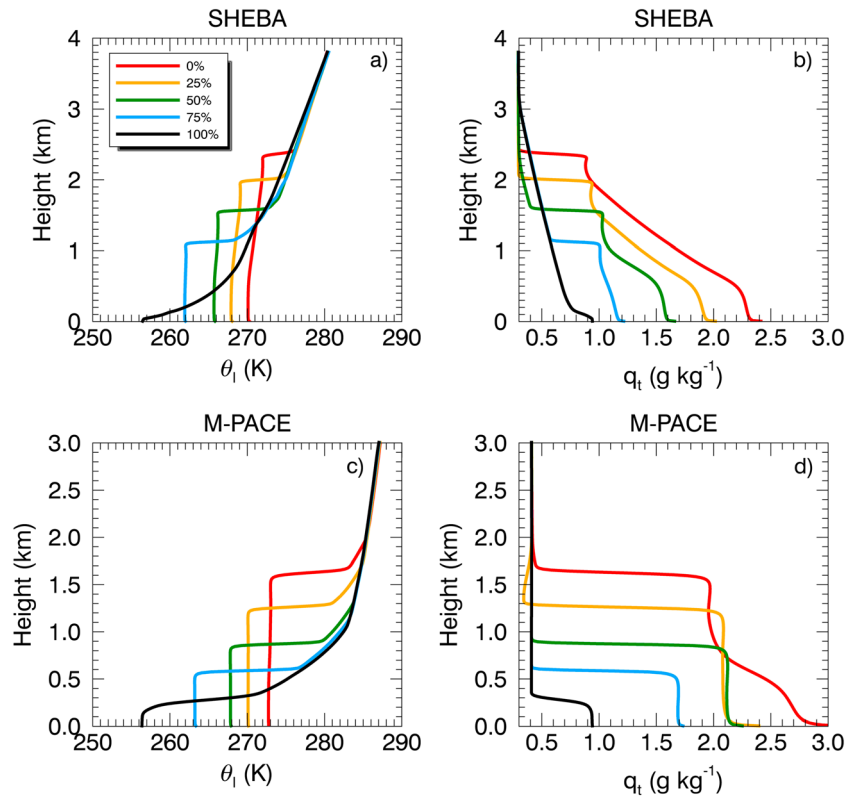


**Figure 9.** Same as Figure 5, but for the SIS simulations averaged over 44–48 h of model output. The colors indicate different simulations.

decreases (Figures 9a, 9b, 10a, and 11a). The 100% sea ice simulation (Figure 11a) is not included in this discussion because of the collapse of cloud layer. The higher cloud top for smaller sea ice cover amount is consistent with our satellite observational analysis (Figure 1), and with Schweiger et al. (2008) over the sea ice margin area, but is not representative of the SHEBA in situ observations that report the highest inversion at 1.2 km during winter when the boundary layer is cold and saturated (Uttal et al., 2002). This suggests that the SIS simulations are analogous to scenarios over the sea ice margin area where the sea ice cover amount may vary significantly from open ocean to various amounts of sea ice cover, provided that the horizontal advection of heat and moisture is small.

The differences between the SHEBA SIS simulations are likely related to changes in the relative importance of turbulent sources according to the TKE budget,

$$\frac{\partial \bar{e}}{\partial t} = \overline{w'b'} - \left( \overline{u'w'} \frac{\partial \bar{u}}{\partial z} + \overline{v'w'} \frac{\partial \bar{v}}{\partial z} \right) - \frac{\partial \overline{w'e'}}{\partial z} - \frac{\partial}{\partial z} \left( \frac{1}{\rho_0} \overline{w'p'} \right) - \varepsilon,$$

where  $e$  is the TKE,  $b$  the buoyancy,  $p$  the pressure, and  $u, v,$  and  $w$  the  $x, y,$  and  $z$ -direction wind components, respectively. The overbar donates the horizontal domain average and the prime the perturbation from the average. The right-hand side terms are the buoyancy production, the shear production, the TKE transport, the pressure work, and the dissipation ( $\varepsilon$ ), which are shown in Figures 12a–12d. As seen from the  $w'b'$  profiles, there are two peaks in buoyancy production, one near the surface and another near the top of the boundary layer. The in-cloud turbulence is mainly driven by cloud top cooling in the higher sea ice simulations (Figure 12g), as also seen from the presence of more negative than positive vertical-velocity skewness within the cloud layer (Figure 11a). The decrease of cloud top radiative cooling with decreasing sea ice increases the importance of the surface turbulence source relative to the cloud top source, as evidenced from the increasing positive vertical-velocity skewness within the cloud layer and the subcloud layer (Figure 11a). However, the surface buoyancy flux ( $w'\theta'_v$ , where  $\theta_v$  is the virtual potential temperature) changes little with sea ice amount (Figure 12e). This weak sensitivity agrees with observations of Sotiropoulou et al. (2014), which

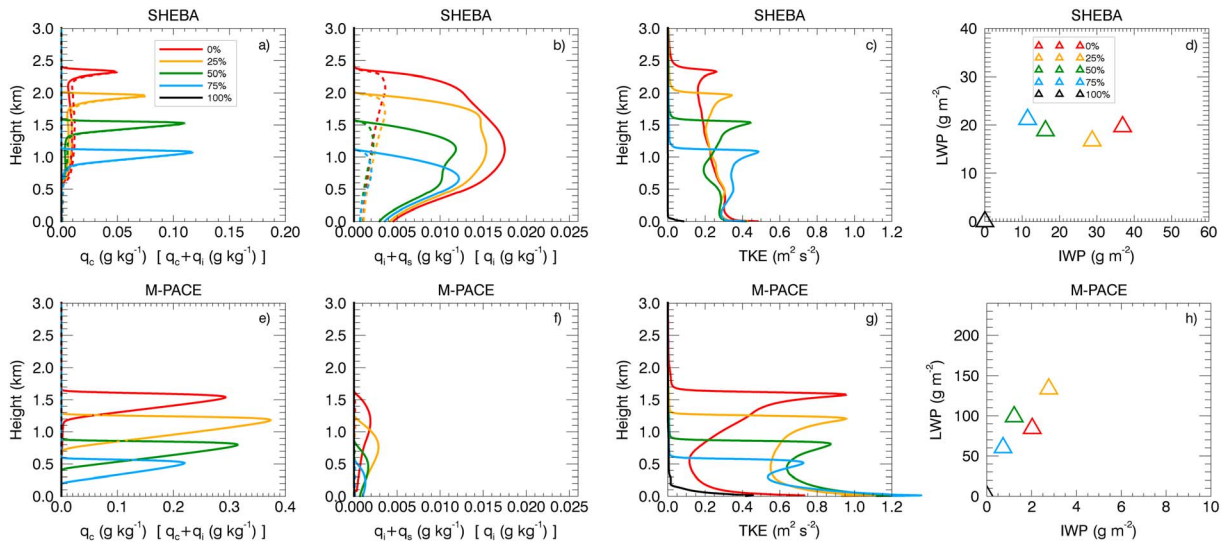


**Figure 10.** Same as Figure 6, but for the SIS simulations averaged over 44–48 h of model outputs. The colors indicate different simulations.

reported that the surface fluxes are very similar for coupled and decoupled boundary layers over the sea ice margin area.

The different SIS simulations share similar vertical structures in the buoyancy and shear productions except that the simulations with smaller sea ice amounts have thicker cumulus layers below the overlying stratocumulus layer. The cumulus cloud layer differs from the overlying stratocumulus layer in that the vertical-velocity skewness is mostly positive in the former whereas it is mostly negative in the latter except for a thin layer of ~50 m thickness near the cloud top (Figure 11a). This thin layer with negative buoyancy and buoyancy TKE production (Figures 12a–12d) is due to entrainment of warm air from above. Within the stratocumulus layer, the less buoyant air is transported downward from the cloud top, resulting in the top-heavy profile of buoyancy flux and the buoyancy production (Figures 12a–12e). Below the cumulus cloud layer, a layer of negative buoyancy with a minimum at ~0.6 km is due to sublimation of precipitating ice (Figure 10b), which is referred to as the decoupling height. This height is associated with the minimum

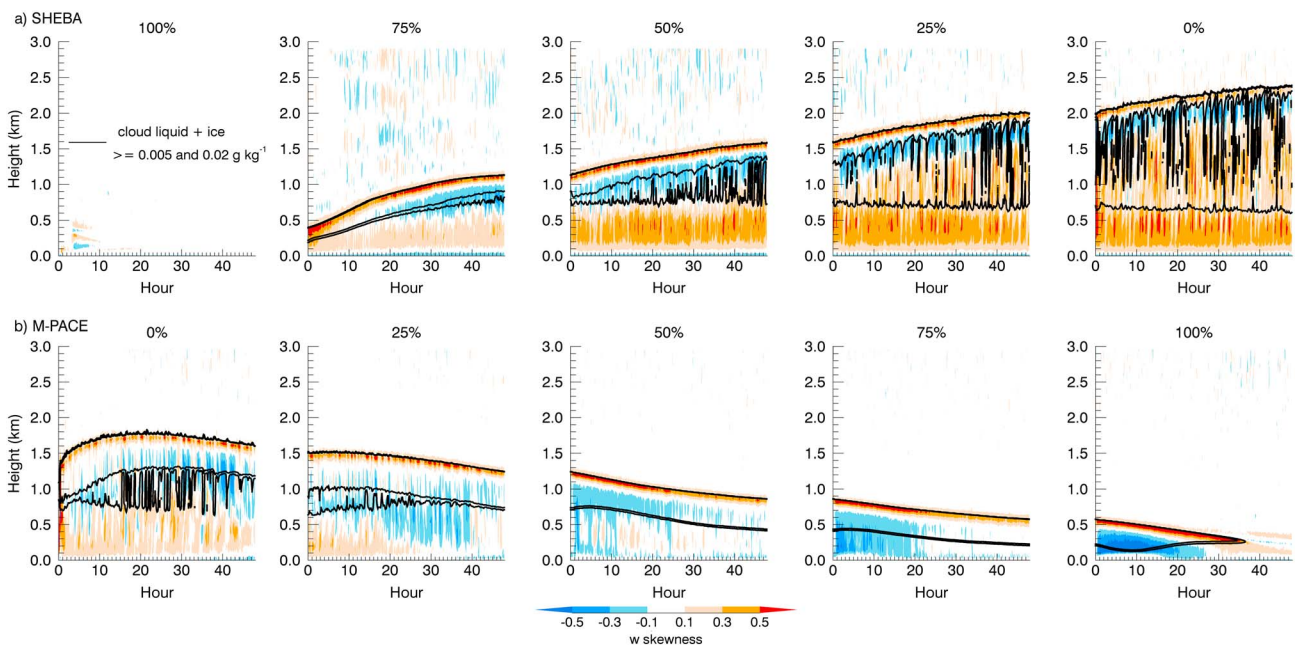


**Figure 11.** Same as Figure 8, but for the (a, upper row) SHEBA and (b, bottom row) M-PACE SIS simulations.

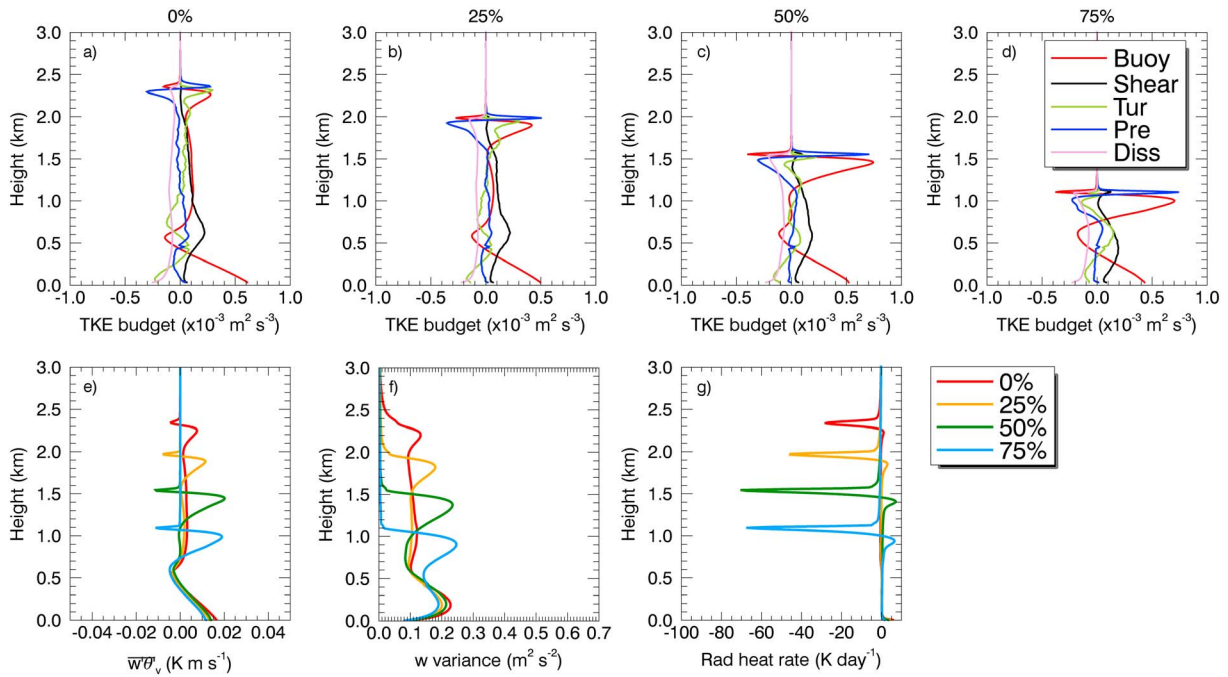


**Figure 12.** For the SHEBA SIS simulations, (a–d) the profiles of model resolved turbulent kinetic energy production due to buoyancy (red), wind shear (black), turbulent transport (green), pressure correlation (blue), and dissipation (pink), (e) turbulent transport of virtual potential temperature (buoyancy flux), (f) vertical velocity variance, and (g) radiative heating (cooling) rate, all averaged over 44–48 h of model output. From Figures 12e–12g, the colors indicate different simulations.

vertical velocity variance ( $\overline{w'^2}$ ). The buoyancy minimum results in negative buoyancy flux ( $\overline{w'\theta'_v}$ ); the shear production (and upward TKE transport to a less degree) tends to cancel out the negative buoyancy production in the 50% and 75% simulations with peaks being slightly below the decoupling height, which reduces the strength of decoupling. The peaks of shear production are located above the decoupling height in the 0% and 25% simulations, while the TKE transports are mostly downward in the lower part of the cumulus layer. Either does not reduce the strength of the decoupling in these two simulations, compared to the 50% and 75% simulations.

The response of M-PACE cloud topped boundary layer to the increase of sea ice cover amount mostly resembles a reverse process of the SHEBA simulations with the decrease of sea ice cover amount. A major difference is that the boundary layers in M-PACE are shallower and more strongly coupled especially for the 50% and 75% sea ice simulations (Figures 9c, 9d, and 11b) than their SHEBA counterparts. The inversion and cloud top height change from 1.6 km (0% sea ice), 1.25 km (25% sea ice), and 0.85 km (50% sea ice) to 0.55 km (75% sea ice) as sea ice increases. The 0% M-PACE simulation has a boundary layer driven by strong cloud top cooling (related to the dominance of liquid water droplets; Figures 10e, 10f, and 10h) and weak surface heating over open ocean (Figure 13a). As the sea ice cover amount increases from 0% to 75%, the SHF and surface buoyancy flux slightly increase instead of decrease in their SHEBA counterparts (Table 1 and Figure 13e). Weakly decoupled boundary layers can be seen from the vertical-velocity skewness for the 0% and 25% simulations (Figure 11b). That is, the updrafts from the surface weaken, the downdrafts from cloud top become narrower and stronger, and the boundary layer becomes fully coupled for the 50% and 75% simulations.

In contrast to SHEBA, the primary source of boundary layer turbulence in M-PACE is the cloud top radiative cooling as indicated by the positive buoyancy production in the entire boundary layer of 25%, 50%, and 75% simulations since the shear production is nearly zero for the entire boundary layer except near the surface (Figures 13a–13d). This is also evident from the profiles of  $\overline{w'^2}$  and  $\overline{w'\theta'_v}$ , which have a maximum near the cloud top and decrease downward to the surface (Figures 13b–13f). In the 0% simulation, the decoupling height is located at ~0.6 km with negative buoyancy production and small  $\overline{w'^2}$ . The turbulent transport of TKE is downward in the upper part of cloud layer and upward in the lower part of the boundary layer for the 25%

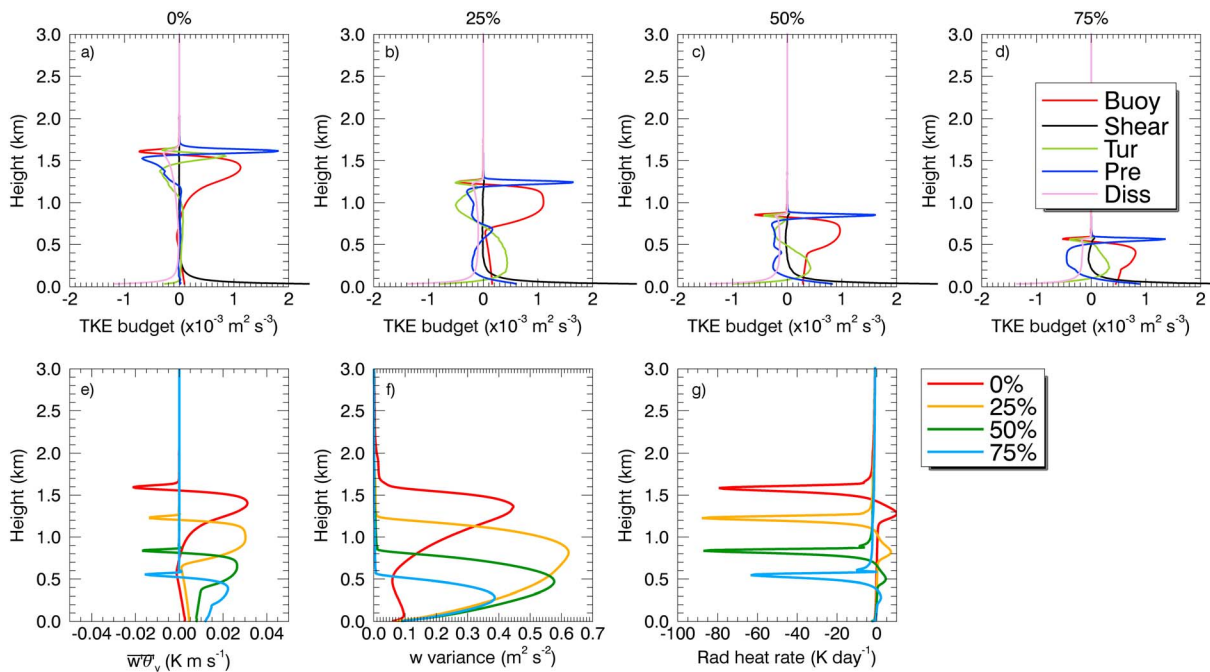


Figure 13. Same as Figure 12, but for the M-PACE SIS simulations.

and 50% M-PACE simulations (Figures 13b and 13c), largely resembling the boundary layer of the 75% SHEBA simulation. Further, the pressure work term is slightly more important within the cloud layer, compared to the 75% SHEBA simulation.

Despite the differences in the boundary layer turbulent characteristics between the SHEBA and M-PACE SIS simulations as discussed above, the difference in boundary layer temperature between two SIS simulations is nearly proportional to that in their sea ice cover amount, for both SHEBA and M-PACE cases. On the other hand, the differences in moisture and turbulent properties within the boundary layer are also influenced by cloud processes, as discussed later. For instance, the boundary layer in M-PACE simulations is always more turbulent and more coupled for the same sea ice cover amount than in the SHEBA simulations. And the buoyancy generation at the cloud top is stronger (Figures 12a–12d and 13a–13d), due to greater cloud top radiative cooling (Figures 12g and 13g) resulting from more opaque clouds associated with larger LWP (Figures 10d and 10h). Thus, the surface turbulent source becomes less important in M-PACE.

### 3.3.2. Cloud Response to the Change of Sea Ice Cover Amount

As discussed above, the AMPS clouds and the boundary layer deepen but the cloud base remains the same as sea ice cover amount decreases in the SHEBA SIS simulations (Figure 10a). The turbulence generated by the surface source grows stronger relative to that generated by the cloud top source. The maximum value of averaged cloud liquid water mixing ratio profile decreases from 0.12 g kg<sup>-1</sup> in the 75% SHEBA simulation to 0.05 g kg<sup>-1</sup> in the 0% SHEBA simulation. The opposite is true for the maximum value of averaged cloud ice mixing ratio profile, increasing from 0.0020 g kg<sup>-1</sup> to 0.0036 g kg<sup>-1</sup> (Figure 10b). To understand these trends, the tendencies of different water species for the 25%, 50%, and 75% simulations are presented in Figure 14a. The cloud ice and snow increase in the entire cloud layer through deposition (dashed blue profiles in Figure 14a), facilitated by the vertical advection of water vapor from below the cloud base (solid black profiles in Figure 14a). The growth of cloud liquid droplets is primarily associated with the turbulence driven by cloud top cooling, evidenced by the peak rate close to the cloud top. The vertical advection of water vapor is due to the buoyancy-generated turbulence driven by the surface source, which increases water vapor in the cloud layer (and then consumed by deposition) but depletes water vapor in the subcloud layer. This mixing becomes weaker as sea ice cover decreases, creating less well-mixed layer in total water mixing ratio (Figure 9b) as the strength of decoupling increases. This result is consistent with observations of Sotiropoulou et al. (2014). As expected, sedimentation decreases cloud ice and snow within the cloud layer but increases them below the cloud base.

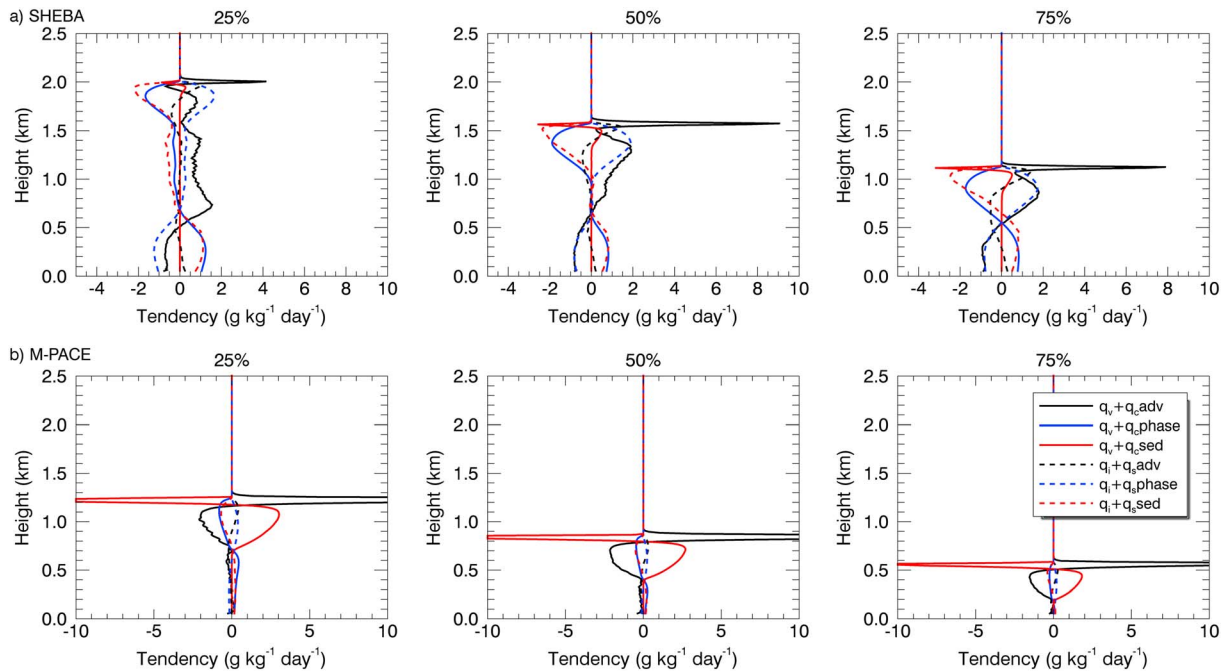


**Figure 14.** For (a, upper row) SHEBA and (b, bottom row) M-PACE simulations, the profiles of water tendency due to vertical advection (black), phase change (blue), and sedimentation (red), averaged over 44–48 h of model output. The solid profiles represent the sum of water vapor and cloud liquid water, and the dashed profiles represent the sum of cloud ice and snow. Within the inversion layer of M-PACE profiles, the maxima of  $q_v + q_c$  tendency due to vertical advection are 49 (25% M-PACE), 35 (50% M-PACE), and 16  $\text{g kg}^{-1} \text{d}^{-1}$  (75% M-PACE), and the minima of  $q_v + q_c$  tendency due to sedimentation are of  $-30$  (25% M-PACE),  $-23$  (50% M-PACE),  $-11 \text{ g kg}^{-1} \text{d}^{-1}$  (75% M-PACE).

Next, we use LWP and IWP, which are integrated over the cloud layer, to concisely discuss the cloud response to sea ice cover variation. For the SHEBA SIS simulations, smaller sea ice cover amounts correspond to greater average IWPs (up to  $37 \text{ g m}^{-2}$  in the 0% SHEBA simulation), but not always greater LWPs (Table 1 and Figure 10d). For the temporal evolution of LWP and IWP, there are larger fluctuations in simulations with smaller sea ice amounts (and the more strongly decoupled boundary layers), due perhaps to the presence of shallow cumulus (Figures 4d and 4e). While the increase of IWP and LWP during the early hours of model integration may reflect the deepening of the cloud topped boundary layer, the decrease of LWP at the later stage is mainly associated with the decrease of cloud liquid within the top most 0.2 km of the cloud layer as the turbulence generated from cloud top weakens (Figure 10a). The decrease of cloud liquid near cloud top may also be caused by (1) the limited moisture source from the surface as the boundary layer becomes strongly decoupled, (2) the drying due to cloud top entrainment (evaporation), and (3) the strong phase change from water vapor to ice.

The shallower and more coupled boundary layers in the M-PACE SIS simulations alter the partitioning between IWP and LWP and their responses to the changes of sea ice cover amount, compared to SHEBA. LWP dominates IWP in all M-PACE simulations (including the reference one), which is only true for the reference SHEBA simulation (Table 1). This is explained from Figure 14b. Within the AMPS cloud layer of the 25%, 50%, and 75% M-PACE simulations, buoyancy-generated turbulence (Figures 13b–13d) induces weak production of cloud ice and snow, which is redistributed vertically by sedimentation and advection (dashed profiles in Figure 14b). The cloud liquid water is generated by turbulence near the cloud top, and it is moved downward through sedimentation as the boundary layer becomes shallower (solid red profiles in Figure 14b), and very small amount of rain is produced (not represented in Figure 14b). The change in LWP/IWP with sea ice cover can also be seen from the longwave cloud radiative effect (CRE), which is defined as the difference between all-sky net longwave radiative flux and clear-sky net longwave radiative flux at the surface. The CRE varies by less than  $5 \text{ W m}^{-2}$  among the 25%, 50%, and 75% M-PACE simulations for the LWP variation of  $73.3 \text{ g m}^{-2}$  between the 25% and 75% simulations. The CRE is much less sensitive to the changes in LWP among the M-PACE SIS simulations compared to the SHEBA SIS simulations (Table 1), probably due to the reduced sensitivity of more opaque liquid clouds associated with large LWPs in the M-PACE simulations.

Thus, the thinner mixed-phase clouds in the SHEBA simulations exert greater impacts on the surface energy budget as sea ice melts (Bennartz et al., 2013).

As demonstrated by both the SHEBA and M-PACE simulations, the responses of AMPS cloud properties to the variation of sea ice cover amount are influenced by microphysical processes and changes of boundary layer turbulent sources. There are some important differences in microphysical processes between the two cases. The cloud ice increases with the decrease of sea ice cover amount in the SHEBA simulations, while the limited moisture source and cloud top entrainment suppress the growth of cloud liquid water. The greater cloud top cooling of AMPS clouds in the M-PACE simulations, due to significantly larger LWP compared to the SHEBA simulations with the same sea ice cover amounts, generates stronger turbulence that reaches all the way to the surface. The lack of moisture advection from below the cloud base in the M-PACE SIS simulations leads to little growth of cloud ice, while the existing cloud ice is removed by precipitation. Another difference between the two cases is that the ice crystal number concentration is significantly smaller in the M-PACE SIS simulations than the SHEBA SIS simulations with the same amount of sea ice cover (Table 1), consistent with the smaller cloud ice mixing ratio and precipitation rate.

#### 4. Summary and Discussion

The responses of the AMPS boundary layer near the sea ice margins to the change of underlying sea ice cover amount have been investigated in this study. We performed two sets of model simulations that mimic the transitions of the Arctic boundary layer resulting from the sea ice cover amount increase and decrease, respectively. The SHEBA and M-PACE simulations have demonstrated that the turbulent sources of the AMPS boundary layer come from cloud top cooling and surface heating. As long as the cloud contains significant amount of liquid water, the cloud top cooling can maintain a well-mixed boundary layer of a few hundred meters driven by buoyancy-generated turbulence. The boundary layer driven by cloud top cooling becomes less coupled to the surface and less well mixed (especially in total water mixing ratio), as the sea ice cover amount decreases, due to the increased surface temperature and deepening of the boundary layer. That is, the decoupling of the cloud layer from the surface may happen over relatively warm sea ice margin areas due to the surface temperature increase as in the SHEBA case and observations (e.g., Sotiropoulou et al., 2014), while over cold sea ice pack, the decoupling is more likely caused by large-scale advection of warmer air as described in Shupe et al. (2013).

On the other hand, increasing the sea ice cover amount lowers the boundary layer height and reduces the relative importance of the turbulence generated at the surface. This allows the boundary layer to be well mixed by turbulence driven by cloud top cooling. This process occurring for the M-PACE simulations with increasing sea ice coverage mostly resembles a reverse process of the SHEBA simulations with decreasing sea ice coverage despite the fact that the M-PACE boundary layers are shallower and dominated by liquid-phase clouds. In either set of simulations, the effect of large-scale advection, which can impact the boundary layer thermodynamic properties and surface SH and LH fluxes, is not included. This, in turn, changes the relative importance of two turbulent sources. The sensitivity to sea ice cover variation found in this study is therefore expected to change.

The changes of liquid and ice water in the AMPS clouds are not in a linear relationship with the variation of sea ice cover amount, although greater IWP is always associated with smaller sea ice coverage in either SHEBA or M-PACE simulations. Their relationship is strongly influenced by microphysical processes and the changes of boundary layer turbulent source. As the sea ice cover amount decreases in the SHEBA simulations, the vertical advection of water vapor spurs the growth of cloud ice and snow, while the limited moisture source suppresses the increase of cloud liquid water. On the other hand, the increase of sea ice cover amount for the M-PACE simulations leads to the dominance of turbulence driven by cloud top cooling in the entire boundary layer, and the significant reduction of moisture supply from the surface, which are further related to the reduction of cloud ice number concentration and IWP.

The change of AMPS cloud properties with sea ice coverage in the sensitivity simulations could be potentially altered by additional source of moisture. Solomon, Shupe, and Persson (2014) have concluded that, for an AMPS boundary layer driven by cloud top cooling, the choice of moisture source from either above or below the AMPS cloud has little impact on LWP, but the removal of both sources would lead to the decay of the AMPS cloud, as also found in this study for the 100% sea ice simulations without large-scale horizontal



advection. For the M-PACE sensitivity simulations, adding large-scale advection of moisture above the cloud top could help maintain the cloud liquid and ice water as the sea ice cover amount increases. On the other hand, the AMPS clouds in the SHEBA simulations may not be significantly different if a moisture source is added above the cloud top, since their moisture source comes from the surface. A careful design of simulations with large-scale advection will be needed to mimic the observed large-scale environments of the Arctic boundary layer to further understand the processes examined in this highly idealized study.

In our simulations, the geometry of sea ice cover prescribed within the domain does not have a significant effect on the relationship between cloud and boundary layer properties and sea ice variation. This is demonstrated by two additional 75% SHEBA and 25% M-PACE simulations, with prescribed sea ice cover along the side of the domain instead of in the center, with other simulation setups unchanged. Compared with their counterparts in the SIS experiments, these two additional simulations are only different in spatial variability, but almost no difference is found in domain-averaged cloud condensate, cloud height and thickness, and turbulent properties.

The results of each simulation with a specific sea ice cover amount are sensitive to the prescribed sea ice and ocean surface temperature. The temporal variation of ocean surface temperature is relatively small compared to the sea ice surface temperature, whereas the sea ice surface temperature depends on the stage of melting, the solar radiation, the internal heat storage of brine pockets, the insulation of accumulated snow over sea ice, and the transfer of heat from the warm ocean below (Semtner, 1976). The changes of boundary layer and cloud properties described in this study are associated with the changes in domain-average surface temperature and fluxes, which are determined by both the percentage of sea ice cover and the prescribed surface temperatures.

This study isolates the effects of sea ice cover amount and the related surface conditions in the AMPS boundary layer near the sea ice margins, which is one of the many components that affect the AMPS. Our results are able to qualitatively explain observed changes in cloud height as a function of sea ice cover amount in relatively well-mixed boundary layers. Studies on the greater Arctic with more integrated processes will benefit from a deeper understanding of the effect of sea ice cover in the boundary layer processes.

#### Acknowledgments

The research was supported by an appointment to the NASA Postdoctoral Program (Zhujun Li) at Langley Research Center, administered by Universities Space Research Association through a contract with NASA, and by a NASA Interdisciplinary Study Project (grant NNH12ZDA001N-IDS; Kuan-Man Xu and Anning Cheng) led by Patrick Taylor. Model simulations used in this study can be accessed through the author by e-mail. Zhujun Li: zhujunlizhujun@gmail.com.

#### References

- Ackerman, A. S., Hobbs, P. V., & Toon, O. B. (1995). A model for particle microphysics, turbulent mixing, and radiative transfer in the stratocumulus-topped marine boundary layer and comparisons with measurements. *Journal of the Atmospheric Sciences*, *52*(8), 1204–1236. [https://doi.org/10.1175/1520-0469\(1995\)052%3C1204:AMFPMT%3E2.0.CO;2](https://doi.org/10.1175/1520-0469(1995)052%3C1204:AMFPMT%3E2.0.CO;2)
- Bennartz, R., Shupe, M. D., Turner, D. D., Walden, V. P., Steffen, K., Cox, C. J., ... Pettersen, C. (2013). July 2012 Greenland melt extent enhanced by low-level liquid clouds. *Nature*, *496*(7443), 83–86. <https://doi.org/10.1038/nature12002>
- Cavalieri, D., Gloersen, P., & Zwally, J. (1990). DMSM SSM/I daily polar gridded sea ice concentrations. In J. Maslanik & J. Stroeve (Eds.). Boulder, CO: National Snow and Ice Data Center. Digital media.
- Collins, W. D., Rasch, P. J., Boville, B. A., Hack, J. J., McCaa, J. R., Williamson, D. L., ... Briegleb, B. (2004). Description of the NCAR Community Atmosphere Model (CAM3.0) (Technical Note TN-464+STR 214 pp.). Boulder, CO: National Center for Atmospheric Research.
- Fan, J., Ovtchinnikov, M., Comstock, J. M., McFarlane, S. A., & Khain, A. (2009). Ice formation in Arctic mixed-phase clouds: Insights from a 3-D cloud-resolving model with size-resolved aerosol and cloud microphysics. *Journal of Geophysical Research*, *114*, D04205. <https://doi.org/10.1029/2008JD010782>
- Francis, J. A., & Hunter, E. (2006). New insight into the disappearing Arctic sea ice. *Eos, Transactions American Geophysical Union*, *87*(46), 509–524. <https://doi.org/10.1029/2006EO460001>
- Fridlind, A. M., van Diedenhoven, B., Ackerman, A. S., Avramov, A., Mrowiec, A., Morrison, H., ... Shupe, M. D. (2012). A FIRE-ACE/SHEBA case study of mixed-phase Arctic boundary layer clouds: Entrainment rate limitations on rapid primary ice nucleation processes. *Journal of the Atmospheric Sciences*, *69*(1), 365–389. <https://doi.org/10.1175/JAS-D-11-052.1>
- Geleyn, J.-F. (1988). Interpolation of wind, temperature and humidity values from model levels to the height of measurement. *Tellus*, *40A*(4), 347–351. <https://doi.org/10.1111/j.1600-0870.1988.tb00352.x>
- Holland, M. M., & Bitz, C. M. (2003). Polar amplification of climate change in coupled models. *Climate Dynamics*, *21*(3-4), 221–232. <https://doi.org/10.1007/s00382-003-0332-6>
- Kato, S., Sun-Mack, S., Miller, W. F., Rose, F. G., Chen, Y., Minnis, P., & Wielicki, B. A. (2010). Relationships among cloud occurrence frequency, overlap, and effective thickness derived from CALIPSO and CloudSat merged cloud vertical profiles. *Journal of Geophysical Research*, *115*, D00H28. <https://doi.org/10.1029/2009JD012277>
- Khairoutdinov, M., & Randall, D. A. (2003). Cloud resolving modeling of the ARM summer 1997 IOP: Model formulation, results, uncertainties, and sensitivities. *Journal of the Atmospheric Sciences*, *60*(4), 607–625. [https://doi.org/10.1175/1520-0469\(2003\)060%3C0607:CRMOTA%3E2.0.CO;2](https://doi.org/10.1175/1520-0469(2003)060%3C0607:CRMOTA%3E2.0.CO;2)
- Klein, S. A., McCoy, R. B., Morrison, H., Ackerman, A. S., Avramov, A., Boer, G. D., ... Zhang, G. (2009). Intercomparison of model simulations of mixed-phase clouds observed during the ARM Mixed-Phase Arctic Cloud Experiment, I: Single-layer cloud. *Quarterly Journal of the Royal Meteorological Society*, *135*(641), 979–1002. <https://doi.org/10.1002/qj.416>

- Krueger, S. K., McLean, G. T., & Fu, Q. (1995). Numerical simulation of the stratus-to-cumulus transition in the subtropical marine boundary layer, Part I: Boundary layer structure. *Journal of the Atmospheric Sciences*, 52(16), 2839–2850. [https://doi.org/10.1175/1520-0469\(1995\)052%3C2839:NSOTST%3E2.0.CO;2](https://doi.org/10.1175/1520-0469(1995)052%3C2839:NSOTST%3E2.0.CO;2)
- Large, W. G., & Pond, S. (1982). Sensible and latent heat flux measurements over the ocean. *Journal of Physical Oceanography*, 12(5), 464–482. [https://doi.org/10.1175/1520-0485\(1982\)012%3C0464:SALHFM%3E2.0.CO;2](https://doi.org/10.1175/1520-0485(1982)012%3C0464:SALHFM%3E2.0.CO;2)
- Moeng, C.-H., & Rotunno, R. (1990). Vertical-velocity skewness in the buoyancy-driven boundary layer. *Journal of the Atmospheric Sciences*, 47(9), 1149–1162. [https://doi.org/10.1175/1520-0469\(1990\)047%3C1149:VVSITB%3E2.0.CO;2](https://doi.org/10.1175/1520-0469(1990)047%3C1149:VVSITB%3E2.0.CO;2)
- Morrison, H., Curry, J. A., & Khvorostyanov, V. I. (2005). A new double-moment microphysics parameterization for application in cloud and climate models, Part I: Description. *Journal of the Atmospheric Sciences*, 62(6), 1665–1677. <https://doi.org/10.1175/JAS3446.1>
- Morrison, H., de Boer, G., Feingold, G., Harrington, J., Shupe, M. D., & Sulia, K. (2012). Resilience of persistent Arctic mixed-phase clouds. *Nature Geoscience*, 5(1), 11–17. <https://doi.org/10.1038/ngeo1332>
- Morrison, H., Pinto, J. O., Curry, J. A., & McFarquhar, G. M. (2008). Sensitivity of modeled Arctic mixed-phase stratocumulus to cloud condensation and ice nuclei over regionally varying surface conditions. *Journal of Geophysical Research*, 113, D05203. <https://doi.org/10.1029/2007JD008729>
- Morrison, H., Zuidema, P., Ackerman, A. S., Avramov, A., de Boer, G., Fan, J., ... Shipway, B. (2011). Intercomparison of cloud model simulations of Arctic mixed-phase boundary layer clouds observed during SHEBA/FIRE-ACE. *Journal of Advances in Modeling Earth Systems*, 3(2), M06003. <https://doi.org/10.1029/2011MS000066>
- Morrison, H., Zuidema, P., McFarquhar, G. M., Bansemer, A., & Heymsfield, A. J. (2011). Snow microphysical observations in shallow mixed-phase and deep frontal Arctic cloud systems. *Quarterly Journal of the Royal Meteorological Society*, 137(659), 1589–1601. <https://doi.org/10.1002/qj.840>
- Palm, S. P., Strey, S. T., Spinhirne, J., & Markus, T. (2010). Influence of Arctic sea ice extent on polar cloud fraction and vertical structure and implications for regional climate. *Journal of Geophysical Research*, 115, D21209. <https://doi.org/10.1029/2010JD013900>
- Perovich, D. K., Richter-Menge, J. A., Jones, K. F., & Light, B. (2008). Sunlight, water, and ice: Extreme Arctic sea ice melt during the summer of 2007. *Geophysical Research Letters*, 35, L11501. <https://doi.org/10.1029/2008GL034007>
- Rienecker, M. M., Suarez, M. J., Gelaro, R., Todling, R., Bacmeister, J., Liu, E., ... Woollen, J. (2011). MERRA: NASA's modern-era retrospective analysis for research and applications. *Journal of Climate*, 24(14), 3624–3648. <https://doi.org/10.1175/JCLI-D-11-00015.1>
- Savre, J., Ekman, A. M. L., Svensson, G., & Tjernström, M. (2015). Large-eddy simulations of an Arctic mixed-phase stratiform cloud observed during ISDAC: Sensitivity to moisture aloft, surface fluxes and large-scale forcing. *Quarterly Journal of the Royal Meteorological Society*, 141(689), 1177–1190. <https://doi.org/10.1002/qj.2425>
- Schweiger, A. J., Lindsay, R. W., Vavrus, S., & Francis, J. A. (2008). Relationships between Arctic sea ice and clouds during autumn. *Journal of Climate*, 21(18), 4799–4810. <https://doi.org/10.1175/2008JCLI2156.1>
- Semtner, A. J. Jr. (1976). A model for the thermodynamic growth of sea ice in numerical investigations of climate. *Journal of Physical Oceanography*, 6(3), 379–389. [https://doi.org/10.1175/1520-0485\(1976\)006%3C0379:AMFTTG%3E2.0.CO;2](https://doi.org/10.1175/1520-0485(1976)006%3C0379:AMFTTG%3E2.0.CO;2)
- Serreze, M. C., Barrett, A. P., Stroeve, J. C., Kindig, D. N., & Holland, M. M. (2009). The emergence of surface-based Arctic amplification. *The Cryosphere*, 2(3), 11–19.
- Serreze, M. C., & Francis, J. A. (2006). The Arctic amplification debate. *Climatic Change*, 76(3–4), 241–264. <https://doi.org/10.1007/s10584-005-9017-y>
- Shupe, M. D. (2011). Clouds at Arctic atmospheric observatories. Part II: Thermodynamic phase characteristics. *Journal of Applied Meteorology and Climatology*, 50(3), 645–661. <https://doi.org/10.1175/2010JAMC2468.1>
- Shupe, M. D., Persson, P. O. G., Brooks, I. M., Tjernström, M., Sedlar, J., Mauritsen, T., ... Leck, C. (2013). Cloud and boundary layer interactions over the Arctic sea ice in late summer. *Atmospheric Chemistry and Physics*, 13(18), 9379–9399. <https://doi.org/10.5194/acp-13-9379-2013>
- Smolarkiewicz, P. K., & Grabowski, W. W. (1990). The multidimensional positive definite advection transport algorithm: Nonoscillatory option. *Journal of Computational Physics*, 86(2), 355–375. [https://doi.org/10.1016/0021-9991\(90\)90105-A](https://doi.org/10.1016/0021-9991(90)90105-A)
- Solomon, A., Shupe, M. D., & Persson, O. (2014). The sensitivity of springtime arctic mixed-phase stratocumulus clouds to surface layer and cloud-top inversion layer moisture sources. *Journal of the Atmospheric Sciences*, 71(2), 574–595. <https://doi.org/10.1175/JAS-D-13-01079.1>
- Solomon, A., Shupe, M. D., Persson, P. O. G., & Morrison, H. (2011). Moisture and dynamical interactions maintaining decoupled Arctic mixed-phase stratocumulus in the presence of a humidity inversion. *Atmospheric Chemistry and Physics*, 11(19), 10,127–10,148. <https://doi.org/10.5194/acp-11-10127-2011>
- Sotiropoulou, G., Sedlar, J., Tjernström, M., Shupe, M. D., Brooks, I. M., & Persson, P. O. G. (2014). The thermodynamic structure of summer Arctic stratocumulus and the dynamic coupling to the surface. *Atmospheric Chemistry and Physics*, 14(22), 12,573–12,592. <https://doi.org/10.5194/acp-14-12523-2014>
- Sotiropoulou, G., Tjernström, M., Sedlar, J., Aichert, P., Brooks, B. J., Brooks, I. M., ... Wolfe, D. (2016). Atmospheric conditions during the Arctic Clouds in Summer Experiment (ACSE): Contrasting open water and sea ice surfaces during melt and freeze-up seasons. *Journal of Climate*, 29(24), 8721–8744. <https://doi.org/10.1175/jcli-d-16-0211.1>
- Stevens, B., Moeng, C.-H., Ackerman, A. S., Bretherton, C. S., Chlond, A., de Roode, S., ... Zhu, P. (2005). Evaluation of large-eddy simulations via observations of nocturnal marine stratocumulus. *Monthly Weather Review*, 133(6), 1443–1462. <https://doi.org/10.1175/MWR2930.1>
- Taylor, P., Kato, S., Xu, K.-M., & Cai, M. (2015). Covariance between Arctic sea ice and clouds within atmospheric state regimes at the satellite footprint level. *Journal of Geophysical Research: Atmospheres*, 120, 12,656–12,678. <https://doi.org/10.1002/2015JD023520>
- Uttal, T., Curry, J. A., McPhee, M. G., Perovich, D. K., Moritz, R. E., Maslanik, J. A., ... Grenfeld, T. C. (2002). Surface heat budget of the Arctic Ocean. *Bulletin of the American Meteorological Society*, 83(2), 255–275. [https://doi.org/10.1175/1520-0477\(2002\)083%3C0255:SHBOTA%3E2.3.CO;2](https://doi.org/10.1175/1520-0477(2002)083%3C0255:SHBOTA%3E2.3.CO;2)
- Vavrus, S., Holland, M. M., & Bailey, D. A. (2011). Changes in Arctic clouds during intervals of rapid sea ice loss. *Climate Dynamics*, 36(7–8), 1475–1489. <https://doi.org/10.1007/s00382-010-0816-0>
- Verlinde, J., Harrington, J. Y., Yannuzzi, V. T., Avramov, A., Greenberg, S., Richardson, S. J., ... Schofield, R. (2007). The Mixed-Phase Arctic Cloud Experiment. *Bulletin of the American Meteorological Society*, 88(2), 205–221. <https://doi.org/10.1175/BAMS-88-2-205>
- Zuidema, P., Baker, B., Han, Y., Intrieri, J., Key, J., Lawson, P., ... Uttal, T. (2005). An Arctic springtime mixed-phase cloudy boundary layer observed during SHEBA. *Journal of the Atmospheric Sciences*, 62(1), 160–176. <https://doi.org/10.1175/JAS-3368.1>